

Numerical Evaluation of Mixing Time in a Tank Reactor Stirred by a Magnetically Driven Impeller

Marina Campolo

Instituto Pluridisciplinar, Universidad Complutense de Madrid, 28040 Madrid, Spain, and Centro Interdipartimentale di Fluidodinamica e Idraulica, Università di Udine, 33100 Udine, Italy

Alfredo Soldati*

Centro Interdipartimentale di Fluidodinamica e Idraulica and Dipartimento di Energetica e Macchine, Università di Udine, 33100 Udine, Italy

In this work, we investigate numerically the mixing characteristics of a tank reactor stirred by a low off-bottom clearance magnetically coupled impeller. We calculate the fully three-dimensional, time-dependent flow field using the Reynolds average form of the Navier–Stokes equations and adopting the sliding mesh approach. Mixing of a scalar species is computed in the Eulerian framework. We compute power consumption, pumping capability, fluid dynamic efficiency, and mixing time to homogeneous distribution from pointwise release of a scalar. We identify relationships useful to optimize the choice of operational parameters. Numerical results are in qualitative agreement with empirical correlations available from the literature and may be used to improve understanding of the mixing processes. The numerical procedure used mimics possible experimental approaches with the advantage of a lower cost. The methodology outlined can be a reference method to derive guidelines for optimization of impeller/tank design and identification of operational parameters.

1. Introduction

Magnetically driven impellers are used to stir reacting fluids whenever complete sealing of the mixture is required for safety or hygiene reasons.

Fields of application range from the chemical industry to pharmaceuticals, food and drinks productions, and to biotechnologies. Depending on the application, the scale of devices may range from 5 to 20 000 L reactors [www.asepco.com, www.mariotti-pecini.it]. Magnetic impellers represent a significant proportion of the overall impeller business (about 15% of the overall revenues [Mariotti and Pecini, private communication]) and increasing research and development efforts are devoted to improve impeller design for specific mixing tasks (e.g., mixing of sensitive products in biotechnology applications).

Despite their economic importance, magnetically driven impellers have received little attention in the literature. To our knowledge, the power input necessary to promote agitation and the time required to complete mixing in magnetically stirred reactors (MSR) have never been investigated, either by experiments or simulations.

The object of this work is to evaluate numerically the fluid dynamic efficiency and mixing time of a reactor stirred by a magnetically coupled impeller in the full range of operative conditions of industrial interest, from laminar to fully turbulent. Our object is to derive relations among operative parameters—power consumption, pumping capability, and mixing time—which can help to optimize operative conditions and, possibly, impeller design.

Even though the physics of mixing does not depend on the way by which motion is transferred from the engine to the impeller, a precise investigation of fluid dynamics and mixing behavior is required before experimental correlations, derived for traditional stirrers, can be confidently used for prediction purposes in MSR.

In this work, we use available computational techniques to reproduce numerically a typical mixing experiment for the impeller under study. Specifically, we simulate the dispersion of a tracer until a uniform concentration is obtained in the vessel. First, we calculate precisely the three-dimensional, time-dependent flow field by solving the Reynolds average form of the Navier–Stokes equations using the sliding mesh (SM) approach; then, we simulate the dispersion of species using a Eulerian–Eulerian approach, considering explicitly the quasi-periodic flow field variations due to impeller rotation.

Numerical simulations are increasingly used to investigate flow field dynamics in complex impeller/vessel geometries. Very accurate predictions of mean and root-mean-square velocity fields have been obtained using Large Eddy Simulation and Direct Numerical Simulation (see refs 1 and 2). The approach proposed here is not new (see, for instance, Bakker et al.³), and yet it is not widely used for the numerical simulation of the mixing process.

In a previous paper,⁴ we have shown that mixing performances depend on the large-scale flow structures generated by impeller rotation and that these structures are time-dependent. Therefore, we believe that the precise evaluation of mixing time must be based on detailed, three-dimensional, time-dependent flow field data, rather than on time-averaged (see ref 5, among others) or time-frozen (see ref 6, among others) flow fields.

* To whom correspondence should be addressed. Tel.: +390432558020. Fax: +390432558027. E-mail: soldati@uniud.it. <http://158.110.32.35>.

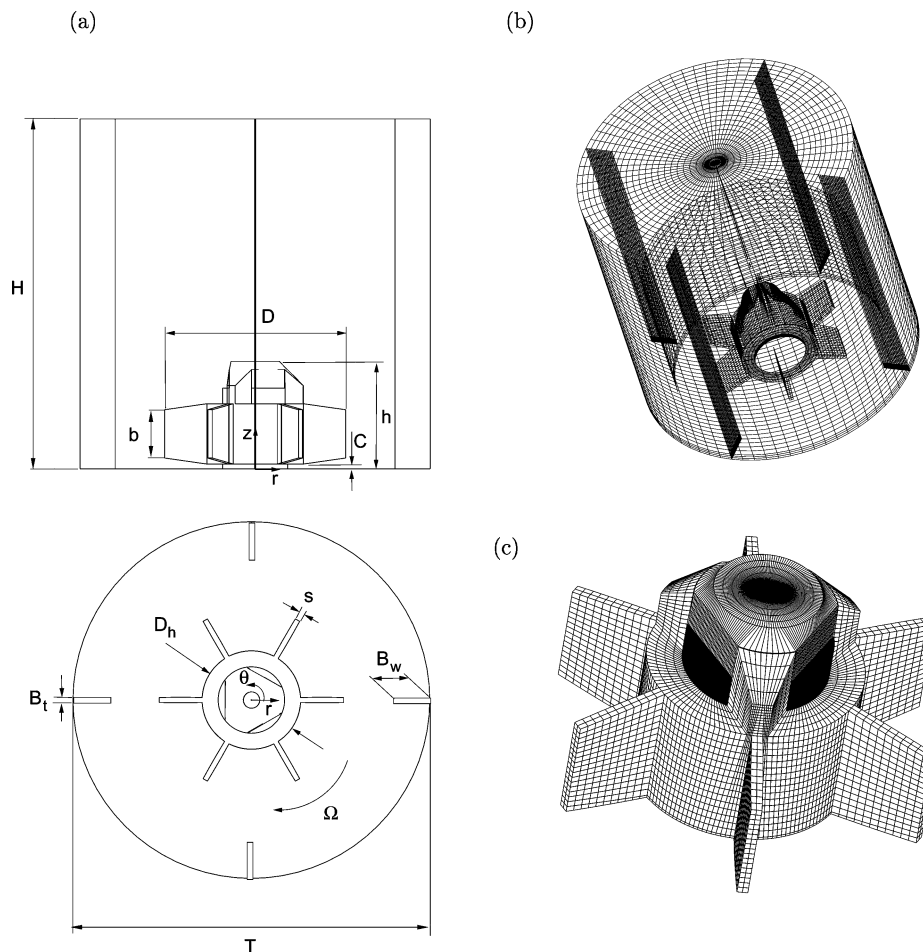


Figure 1. Geometric configuration of a magnetic stirred reactor: (a) side and top view with reference coordinate system, (b) computational domain, and (c) details of impeller. Geometric dimensions are shown in Table 1.

We perform the—numerical—mixing experiment when the flow in the tank is fully developed. In real experiments, this choice ensures reproducibility of results; in our numerical experiments, this choice allows exploitation of the hybrid approach^{4,7} for the calculation of the fully developed flow field, avoiding explicit simulation of the start-up of agitation.

We analyze in detail the flow field dynamics and we evaluate power consumption, pumping capability, and pumping efficiency at different flow regimes. Then we calculate the mixing time^{8–10} and discuss our results against correlations available from the literature.^{11,12} Numerical results are in qualitative agreement with existing correlations derived for traditional impellers.

2. Methodology

2.1. Geometry. Figure 1a shows the flat bottom, cylindrical vessel (19 L capacity) investigated in this work. The tank is perfectly sealed and filled with the working fluid. The six-blade impeller is placed at the bottom of the tank and is magnetically coupled to the external engine (clockwise rotation); four baffles are placed symmetrically at the wall of the tank to improve the top–bottom turnover. Figure 1a shows also the reference cylindrical coordinate system, centered at the bottom of the tank, and Table 1 summarizes the geometric dimensions of the vessel and impeller.

2.2. Simulations. The numerical simulations performed in this work span the full range of working conditions of industrial interest, corresponding to Rey-

Table 1. Geometric Dimensions of Vessel and Impeller

Vessel/Impeller Data					
vessel diameter	T	290 mm	impeller diameter	D	150 mm
vessel height	H	290 mm	impeller height	h	85 mm
baffle width	B_w	29 mm	blade height	b	40–50 mm
number of baffles	n_B	4	number of blades	n_b	6
baffle thickness	B_t	3 mm	blade thickness	s	4 mm
clearance	C	5 mm	hub diameter	D_h	80 mm

Table 2. Fluid Properties and Angular Velocities used in Numerical Experiments: Reynolds Numbers are in the Range $10–10^6$

	Re	ρ [kg/m ³]	μ [Pa·s]	N [rpm]
S1	1.125×10^1	1000	10	300
S2	1.125×10^2	1000	1	300
S3	1.125×10^3	1000	0.1	300
S4	1.125×10^4	1000	0.001	30
S5	1.125×10^5	1000	0.001	300
S6	1.125×10^6	1000	0.001	3000

nolds number, $Re = \rho ND^2/\mu$, in the range $10–10^6$. Table 2 shows the values of density, ρ , viscosity, μ , and angular velocity, N (rpm), chosen for the simulations.

We chose to use different fluids for simulations performed at low Reynolds numbers (simulations S1–S3 of Table 2) and at larger Reynolds numbers (simulations S4–S6). For simulations S4, S5, and S6, performed in the fully turbulent regime ($Re > 10^4$), the fluid is water and we obtain different Reynolds numbers, changing the angular velocity; for simulations S1, S2, and S3, performed at $Re < 10^4$, the density (1000 kg/m³) and angular velocity are fixed (300 rpm) and we

obtain different Reynolds numbers, changing only the fluid viscosity.

Fluids used for simulations S1–S3 are characterized by the same density of water and viscosities typically found in food productions (from 10 Pa·s of honey to 1 Pa·s of syrups and to 0.1 Pa·s of oil–water emulsions). These specific choices should not affect our results since, following Rushton,¹³ for baffled tanks (i.e., when effects of surface deformation are negligible) the Reynolds number is the only parameter controlling the fluid behavior.

2.3. Methodology. We calculate the three-dimensional, time-dependent flow field using a finite-volume, commercial code (Star-CD) which solves the Reynolds average form of mass and momentum balance equations for the fluid in the tank. Figure 1b shows the computational domain, made of 212 530 finite volumes (161 418 in the impeller region and 51 112 in the rest of the tank) and the complex shape of the impeller (see Figure 1c). Boundary conditions are no slip at solid surfaces (wall of the tank and rotating impeller). For simulations S4–S6, corresponding to a turbulent regime, we account for the effect of turbulent fluctuations using a $k-\epsilon$ model complemented by the algebraic “law of the wall”.^{14,15} Preliminary grid sensitivity analysis ensured that the domain discretization shown in Figure 1b was refined enough to obtain grid-independent results. Specifically, we found a maximum difference equal to 4% for the flow field calculated at pseudo steady state using the grid shown in Figure 1b and a grid 2 times more refined in the impeller region.

We chose to calculate the flow field at each incremental position of the impeller, exploiting a transient, sliding mesh (SM) approach (see ref 16 for details). This precise flow field characterization allows numeric reproduction of the time-dependent mixing processes with adequate accuracy. For the reproducibility of our results, we chose to investigate the dispersion of species in the fully developed flow (pseudo steady state conditions). These conditions are extremely costly and time-consuming to reproduce using full transient computations since, in the real apparatus, order 30 impeller revolutions are necessary to achieve pseudo steady state starting from fluid at rest. In this work, we avoid the explicit simulation of the start-up of agitation using the hybrid approach. First, we calculate an approximate flow field using the multiple frame of reference (MFR) approach;^{4,17} second, we use this flow field as a starting condition for the sliding mesh simulation.^{4,18} By monitoring continuously the variation of power consumption, upward flow rate, and azimuthal momentum, we find that five impeller revolutions with SM are sufficient to achieve pseudo steady state starting from the MFR solution. The calculation of the fully developed flow field required an overall CPU time of about 50 h on a 2×800 MHz processors, 1 GB RAM server, for each examined condition.

At pseudo steady state, we release the tracer and then solve for the mass balance equation of the injected species using the Eulerian–Eulerian approach. We chose to use a passive tracer to tag the spreading of fluid as in a dye injection experiment. Density and viscosity are the same as the base fluid. In these conditions, the amount of injected tracer and its physical properties have no effect on mixing time. We follow the spreading of the tracer, monitoring continuously the values of concentration at different sampling points. From our

results, the concentration at sampling locations becomes steady after about 16 impeller revolutions. The calculation of the dispersion of species up to well-mixed conditions required about 150 h of CPU time on the same server for each examined condition.

3. Results

3.1. Flow Field Analysis. The shape of the impeller and the low value of the off-bottom clearance have a large influence on the flow field generated in the tank. Figure 2 shows snapshots of the flow field calculated at four vertical sections of the reactor. Considering the coordinate system shown in Figure 1a, sections are taken at $\theta = 0, 30, 60,$ and 90° , corresponding to different relative positions of baffles and impeller blades.

Consider first Figure 2a, representing the flow field in the section $\theta = 0^\circ$. Vectors represent radial and vertical components of velocity for simulation S5 of Table 2 and pseudo steady state conditions. At the time considered, blade and baffle are aligned in this section and regions without vectors identify the part of the section corresponding to the impeller (on the left) and the baffle (on the right). In the region above the blade, the flow moves downward, driven by the low pressure generated by the rotating impeller. The impeller accelerates the fluid, which is discharged radially and downward at blade tip, with an inclination angle of about -45° with respect to the axial direction, z . Below the impeller, the discharged jet impinges on the tank bottom and then is redirected in the radial direction. The radial flow moves to the baffle where it separates in two streams, moving in the two azimuthal directions, respectively upstream and downstream the baffle.

The right part of Figure 2a shows streamlines corresponding to the vector field. Iso-contours are 0. (solid line), -0.01 , -0.005 , and -0.001 (dashed lines) and 0.001 , 0.005 , and 0.01 (dash-dotted lines). We observe that the fluid discharged from the impeller generates circulation in the region between the blade and the baffle. Near the baffle, the fluid moves upward to the top of the tank, turns toward the rotation axis, and then, above the blade, goes downward toward the impeller. This bottom-up circulation is strong only in the lower part of the vessel ($h/H \leq 0.3$), whereas the upper part of the tank is characterized by slow fluid motion.

Consider now Figure 2b, corresponding to the section $\theta = 30^\circ$, between two blades and behind the baffle. The downward moving flow hits vertically the bottom wall, losing a lot of energy, and then deviates radially, generating a strong circulation which extends toward the side wall of the tank and upward, toward the upper part of the vessel. Near the wall, we observe a dead zone of flow, indicated by the zero streamline iso-contour. In this region, the flow opposes the upward circulation of fluid which is broken into two loops.

Considering Figure 2c, corresponding to section $\theta = 60^\circ$, aligned with the impeller blade, we can observe that the blade deflects radially the axial downward flow, and bottom-up circulation is enhanced by the absence of the baffle.

Finally, consider Figure 2d, corresponding to section $\theta = 90^\circ$, for which the baffle is equally distant from the two blades. The axial, downward flow hits the bottom wall and deviates radially, and the baffle opposes the circulation of fluid, which is strong only in the lower part of the vessel.

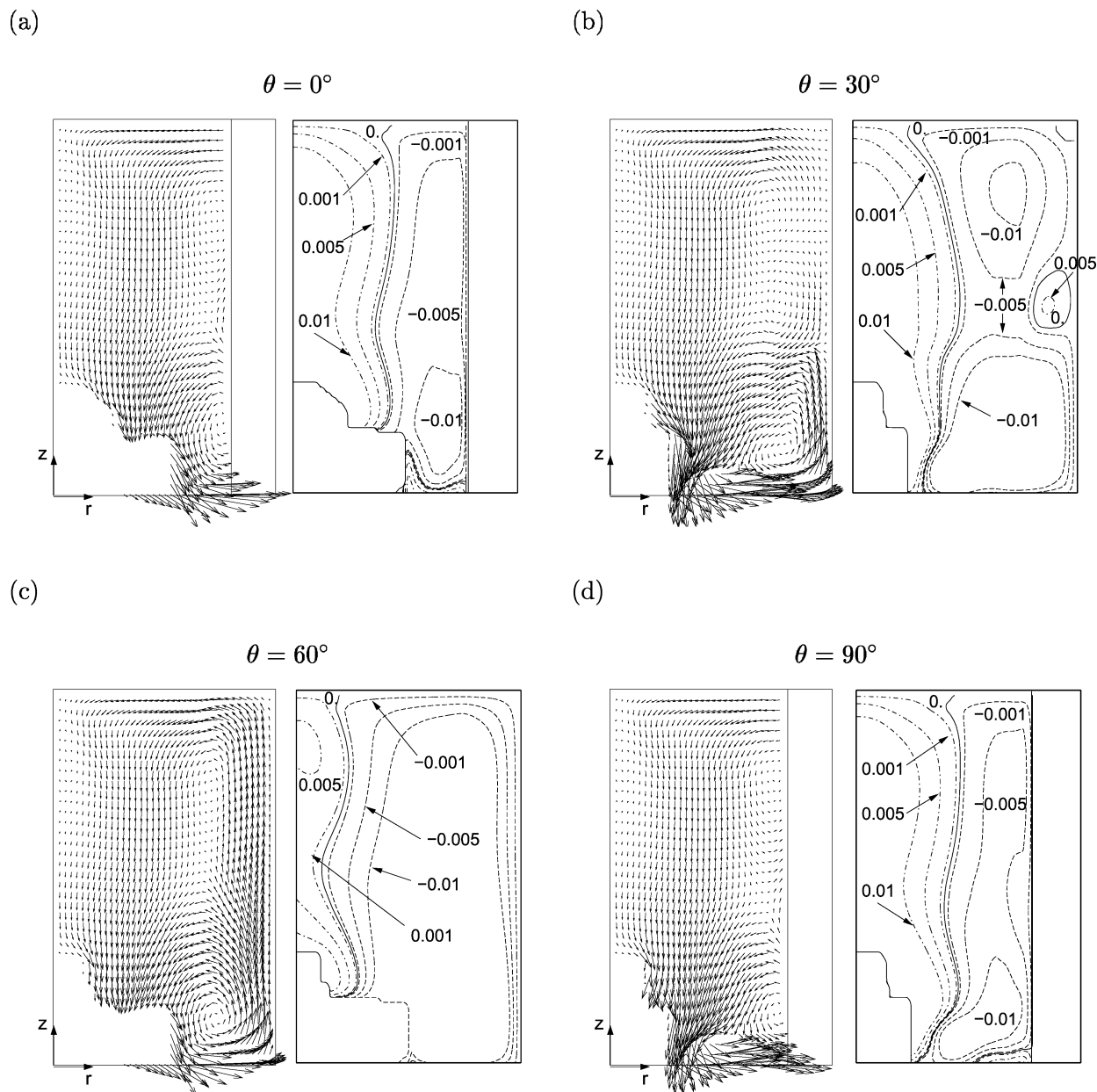


Figure 2. Flow field and streamlines calculated for simulation S5 of Table 4 in four vertical sections of the reactor: (a) $\theta = 0$, (b) 30, (c) 60, and (d) 90°. Snapshots correspond to fully developed flow.

These observations underline two main characteristics of the flow in this impeller/vessel configuration. First, the impeller produces strong circulation in the lower part of the tank. Circulation extends up to the top of the tank in the regions between baffles, where the discharge stream leaving the blades is deflected upward at the tank wall. Considering three-dimensional, time-dependent effects, the flow discharged by the impeller generates a pulsating, toroidal vortex which is responsible for the transport of fluid in the bulk of the tank. Second, a significant part of the energy that the fluid gains from impeller rotation is dissipated at the bottom of the tank. As reported by Armenante et al.,¹⁹ this effect, known as throttling effect, is usually observed in low off-bottom clearance impellers: the smaller the impeller clearance, the more abrupt the change in flow direction, which generates more turbulence and corresponds to increased power consumption. These two issues need to be investigated further from the perspective of impeller performance optimization.

3.2. Characteristic Curves. (a) Power Input. We characterize impeller performances by calculating power input and pumping flow rate at pseudo steady state for each simulated condition. In previous works,²⁰ power consumption was calculated from the total dissipation of power in the entire fluid volume. Following Verzicco et al.,² given the different time scales of the fluid structures generated by the rotating impeller, it is very difficult for RANS models to parametrize correctly all the flow fluctuations and reproduce precisely the kinetic energy and dissipation profiles. Thus, rather than integrating the dissipation of energy in the fluid volume, we decided to calculate the power input, P , as the torque on the impeller blades, multiplied by the angular velocity,

$$P = \omega \int_A \mathbf{r} \times \boldsymbol{\tau} dA \quad (1)$$

where A is the overall impeller surface, ω is the angular velocity vector (rps), \mathbf{r} is the position vector, $\boldsymbol{\tau}$ is the

Table 3. Power Consumption, Discharge Flow, Circulation Flow and Corresponding Dimensionless Numbers for Numerical Experiments

	Re	P [W]	q_d [kg/s]	q_c [kg/s]	Ne	N_{qd}	N_{qc}	η
S1	1.125×10^1	47.532	2.81	3.73	5.01	0.166	0.219	0.033
S2	1.125×10^2	39.47	7.13	9.28	4.168	0.423	0.550	0.101
S3	1.125×10^3	35.54	7.92	12.24	3.744	0.468	0.723	0.125
S4	1.125×10^4	0.03643	0.89	1.48	3.838	0.527	0.877	0.137
S5	1.125×10^5	36.56	8.83	14.6	3.85	0.523	0.865	0.135
S6	1.125×10^6	36.84×10^3	88.36	145.7	3.88	0.524	0.863	0.134

stress tensor, and dA is the infinitesimal surface. We believe that velocity gradients at solid surfaces are simulated better than turbulent quantities, and this ensures higher confidence in the results.

Table 3 reports calculated values of power input and corresponding values of dimensionless power number, $Ne = P/\rho N^3 D^5$. Figure 3a shows the values of Ne (solid symbols) versus Reynolds number, Re . As usually observed for traditional, shaft-driven reactors, the profile of the power number versus the Reynolds number, $Ne = Ne(Re)$, changes from laminar ($Re < 10^3$) to turbulent ($Re > 10^3$) conditions. For $Re > 10^4$, the power number becomes independent of the Reynolds number and equal to a constant, asymptotic value of $Ne = 3.85$.

We compare our results with the power characteristic curve of Nagata,²¹ indicated by a dotted line in Figure 3a. To calculate the parameters of the Nagata curve,²¹ we adapted the correlations derived for paddle impellers to our impeller/vessel configuration, as reported in the Appendix. From these correlations, we obtain $Ne = 3.71$ in the fully turbulent regime, which is in good agreement with 3.85 calculated numerically. The agreement between the Nagata curve²¹ and our calculations deteriorates in the laminar regime (the difference is 6% for simulation S2 and up to 100% for simulation S1), where

simulations calculate lower power input values. At present, we have no explanation for the observed behavior.

The power number value in fully turbulent conditions is comparable to that of traditional impellers (e.g., it is $Ne = 4.8$ for a standard six-blade Rushton impeller), and it is larger than that of efficient industrial impeller configurations (e.g., it is $Ne = 0.7$ and 0.9 for retreated curved blade and turbofoil turbine impellers, as reported in ref 22). This suggests that power input reduction may be a relevant point for the optimization of performances of the present impeller/vessel configuration.

(b) Pumping Capability. We evaluate the stirring produced in the vessel equipped with the magnetic impeller calculating the discharge flow, q_d (kg/s), and the circulation flow, q_c (kg/s).

The discharge flow measures the flow rate of the submerged jet generated by the impeller and is customarily used to evaluate impeller performances. We calculate the discharge flow integrating the radial component of velocity over the minimal cylindrical surface coaxial with the impeller and enclosing the blades, extending from the bottom of the vessel to the height of the blade tip, $z = 60$ mm. Table 3 shows values of q_d and the corresponding values of the dimensionless discharge flow number, $N_{qd} = q_d/\rho ND^3$.

The secondary circulation flow measures the top-bottom turnover and is customarily used to evaluate the mixing time. We calculate the secondary circulation flow integrating the flux directed upward across a reference section normal to the rotation axis at $z = 7/3$, just above the impeller. Table 3 shows values of q_c and corresponding values of secondary circulation flow number, $N_{qc} = q_c/\rho ND^3$.

Figure 3b shows values of N_{qd} and N_{qc} versus Reynolds number. N_{qd} and N_{qc} increase for increasing Re . In the range of Reynolds numbers considered, the ratio of circulation flow number to discharge flow number increases from 1.3 to 1.67, indicating that the submerged jet discharged from the impeller is able to entrain surrounding fluid and to transfer motion from the impeller region to the rest of the tank. Furthermore, values of N_{qd} and N_{qc} in the fully turbulent regime are comparable to those calculated for efficient industrial impellers ($N_{qd} = 0.35$ for retreated curved blade impeller and $N_{qd} = 0.56$ for turbofoil turbine, see ref 22), indicating that pumping capability seems to be not a critical point for impeller performances.

(c) Fluid Dynamic Efficiency. The fluid dynamic efficiency, i.e., the balance between agitation and costs, is customarily used to evaluate impeller performances in industrial applications. Fluid dynamic efficiency is defined as pumping capability per unit of power input and can be calculated as $\eta = N_{qd}/Ne$. Table 3 shows values of η for the MSR, and Figure 3c plots values of η versus Re . We observe that η becomes steady around a value of 0.135 in the fully turbulent regime. Values of

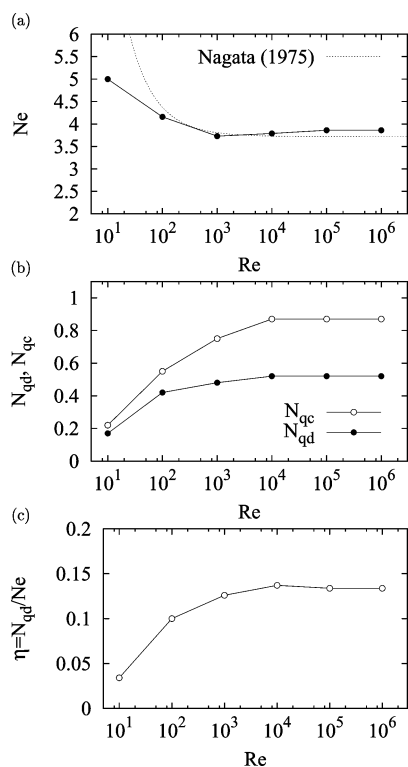


Figure 3. Characteristic curves for MSR: (a) power number versus Reynolds number (symbols are calculated values, dotted line is power characteristic from Nagata, 1975), (b) circulation and discharge flow numbers versus Reynolds number, and (c) fluid dynamic efficiency versus Reynolds number.

η are lower than those for other impeller/tank configurations,²² indicating that even though the impeller transfers motion to the fluid, as shown by large values of the secondary circulation number, this effect is obtained with large power consumption. As observed in section 3.1, the flow elaborated by the impeller is abruptly deflected at the bottom wall. The energy dissipated in this way may account for the high-power input required to maintain impeller rotation. Optimized impeller shape, able to promote a more gradual transition of the flow from the axial to the radial direction, would probably improve impeller performances.

3.3. Mixing Time. (a) Numerical Experiment. In many mixing applications, the object of design is to reduce the time to achieve complete mixing, rather than to increase the fluid dynamic efficiency. Mixing time, θ_{mix} , defined as the time necessary to achieve a certain degree of homogeneity in the stirred vessel (for example, 95% of the perfectly mixed value) is evaluated introducing a tracer into the vessel and monitoring its dispersion (i.e., the local variation in concentration) at sampling locations.

In this work, we evaluate the mixing time numerically, reproducing exactly the real experiment. At time \bar{t} (corresponding to fully developed flow), we inject instantaneously in the tank a finite volume of tracer, V_0 , of starting concentration, C_0 . We solve the mass transport equation using the flow field calculated by the full-transient SM simulation in the different working conditions of industrial interest.

As shown by many investigations on segregation phenomena in stirred tanks, there is experimental evidence that the point of injection influences the mixing of tracers (see ref 23, among others). In this work, we consider the dispersion of tracers injected at different starting positions. Specifically, we simulate the simultaneous dispersion of three tracers. Figure 4 shows the positions of injection points. Tracer 1 is released at $2r/T = 0.66$, $\theta = 195^\circ$, and $z/T = 0.1$; tracer 2 is released at $2r/T = 0.66$, $\theta = 320^\circ$, and $z/T = 0.53$; and tracer 3 is released at $2r/T = 0.37$, $\theta = 110^\circ$, and $z/T = 0.92$. We chose these injection points based on the flow field analysis presented in section 3.1. For tracer 1, released in the impeller discharge stream, we expect fast convective transport and complete mixing; for tracer 2, released in the downward axial flow moving from the upper part of the vessel toward the impeller, we expect delayed convective transport and, yet, complete mixing; for tracer 3, released at the top of the vessel, we expect extremely delayed convective transport.

Figures 5a–d show the dispersion over time of tracer 1. Results refer to simulation S5 in Table 4 and snapshots are taken at times $t = 0.02, 0.2, 0.6,$ and 1.6 s after release, corresponding to 0.1, 1, 3, and 8 revolutions. The first two snapshots show different impeller positions. Figures 5e–h and Figures 5i–n show the dispersion of tracers 2 and 3 at the same time instants and for the same simulation. We visualize the evolution of dispersion by identifying the regions of the fluid where the tracer concentration is larger than $C_m/0.95$ using a gray surface (i.e., the concentration isosurface $C = 1.05 \cdot C_m$). Here, C_m is the perfectly mixed value calculated as $C_m = C_0 V_0 / V_{\text{vessel}}$, where V_{vessel} is the volume of the fluid in the tank (18.75 L, considering the volume of the working fluid only).

Consider first Figures 5a–d, describing the dispersion of tracer 1. The starting blotch of fluid is stretched

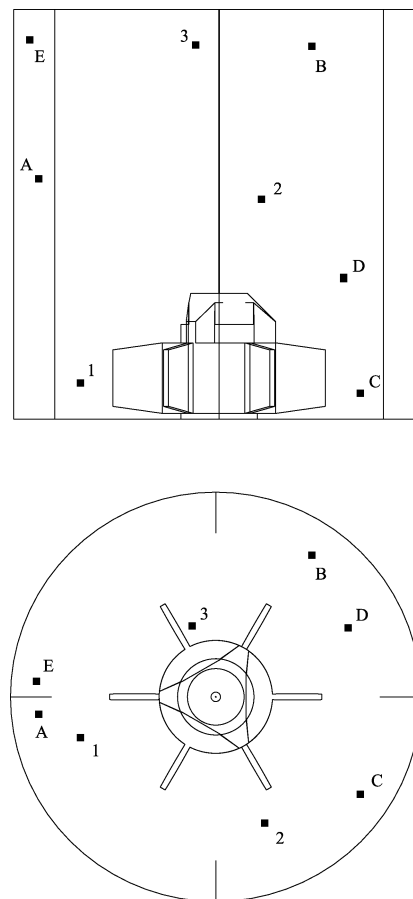


Figure 4. Positions of tracers injection points and monitoring points: tracer 1 is released at $2r/T = 0.66$, $\theta = 195^\circ$, and $z/T = 0.1$; tracer 2 is released at $2r/T = 0.66$, $\theta = 320^\circ$, and $z/T = 0.53$; and tracer 3 is released at $2r/T = 0.37$, $\theta = 110^\circ$, and $z/T = 0.92$. Monitoring points are located at various distances from injection points to obtain dispersion data representative of average transport of mass in the vessel.

counterclockwise by the jet discharged from the impeller, which is moving radially toward the wall of the tank (Figure 5a). When the blotch reaches the baffle, it branches into two parts which follow different patterns (Figure 5b). The blotch upstream the baffle expands vertically toward the top of the tank, driven by the upflow circulation which has maximum intensity at this position; when at the top of the vessel, the blotch transpasses the baffle in the direction of the rotating flow (Figure 5c). The blotch downstream the baffle avoids the mid-height recirculating zone behind the baffle (see Figure 2b) and moves toward the side wall and the bottom of the tank, driven by the toroidal vortex responsible for secondary circulation in the vessel. Near the baffle placed at $\theta = -90^\circ$, the toroidal vortex is compressed (see Figures 2a and d), and the tracer is driven again into the impeller region, where it is accelerated toward the baffle. After 8 impeller revolutions (see Figure 5d), the tracer has spread into a large part of the vessel.

Consider now Figures 5e–h describing the dispersion of tracer 2. The starting blotch of fluid is stretched downward in the axial direction and disperses only to a reduced extent compared with tracer 1. Dispersion is enhanced when the downward moving blotch reaches the impeller. After 8 impeller revolutions (see Figure 5h), the tracer has spread in a volume of the vessel comparable to that occupied by tracer 1.

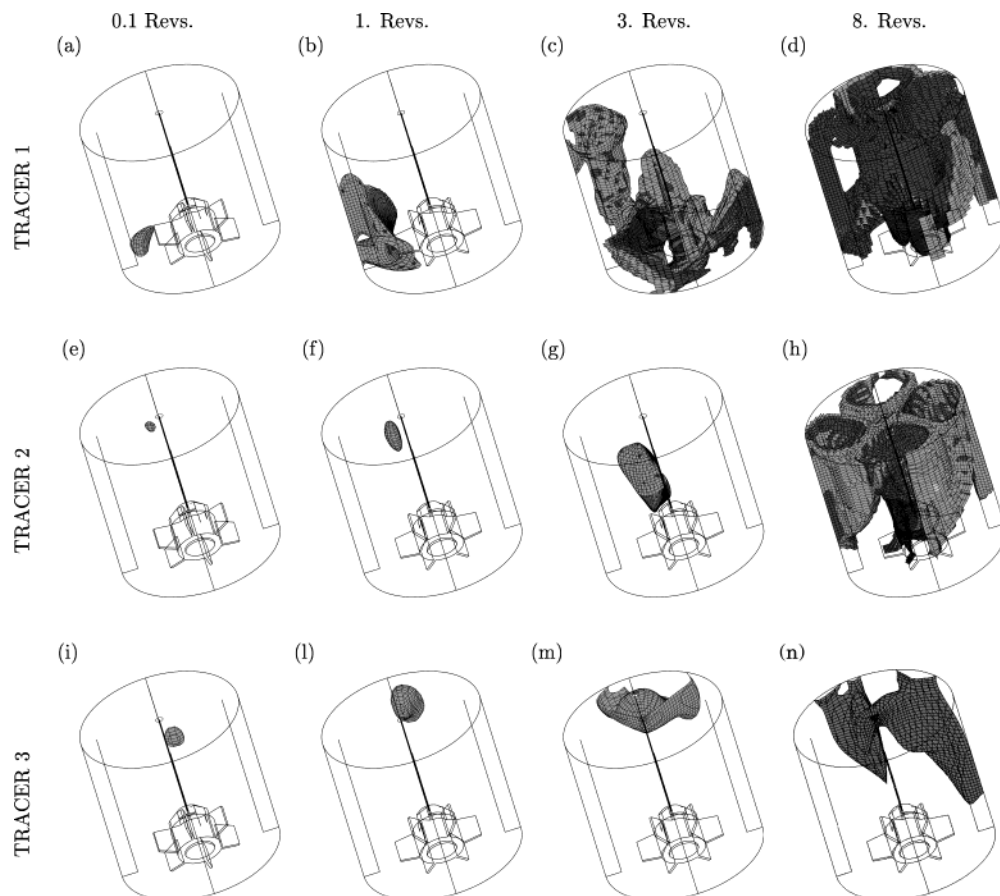


Figure 5. Spreading of scalars after 0.1, 1, 3, and 8 revolutions for simulation S5 in Table 2: (a)–(d) injection point 1, (e)–(h) injection point 2, and (i)–(n) injection point 3. Surfaces identify regions where $C > 1.05 \cdot C_{\text{mix}}$.

Consider finally Figures 5i–n describing the dispersion of tracer 3. The starting blotch of fluid disperses only slightly and remains confined in the upper part of the tank for a long time (see Figures 5i–h). For this tracer, the possibility to disperse in a large volume of the tank is delayed until the tracer is convected either in the region above the blades, which is slowly moving downward, or in the region behind the baffle ($\theta = 0^\circ$), where the upper loop of the secondary circulation (see Figure 2b) may transport the tracer downward toward the wall of the tank.

(b) Concentration Curves. In real experiments, the value of the mixing time is derived from the analysis of the concentration evolution at a few reference points only. In this work, we monitored continuously over time the local value of concentration at five points in the vessel, indicated as A, B, C, D, and E in Figure 4. Monitoring points are located at various distances from injection points to obtain dispersion data representative of the average transport of mass in the vessel.

Figure 6a shows the evolution of concentration for tracer 1 during the mixing experiment considered in Figure 4 ($Re = 1.26 \times 10^5$). Concentration values are normalized using the well-mixed value, C_m . Consider first the evolution of concentration at point A, which is near the point of injection, at mid-height in the tank. We observe a small peak of concentration soon after two revolutions and a larger peak after six revolutions. Then the concentration becomes steady at the perfectly mixed value. Following Patwardhan and Joshi,⁵ the time between two peaks in the concentration plot measures the time of circulation, i.e., the time required for tagged fluid particles to run twice through the same position

in the tank. In experiments, the mixing time is taken as a multiple (three to five times) of the time of circulation. Consider now the concentration profile at point C, which is far from the injection point 1 and, yet, in the impeller stream region. We find the first peak in concentration at the same time of point A, but the peak value is more than 8 times larger, indicating that a larger amount of tracer is moving into the region of point C. Concentration decreases slowly in the following revolutions due to dispersive effects, approaching the perfectly mixed, steady value. We observe similar concentration profiles for monitoring points B, D, and E. Differences are in the value of concentration at the peak and in the time at which the peak is observed. Concentration profiles at all monitoring points became steady around the perfectly mixed value within 15 impeller revolutions.

Consider now Figure 6b, showing the evolution of concentration for tracer 3 during the same experiment. In this case, dispersion is initially confined in the upper part of the vessel, as indicated by concentration profiles at points C, D, and B characterized by large peaks after five, six, and seven revolutions. Peak values, larger than those observed for tracer 1 at later times, indicate that both convective effects and dispersive effects are reduced for tracer 3. However, after 15 revolutions, concentration profiles at all monitoring points reach the steady state value.

Figures 6c and d show the evolution of concentration for tracers 1 and 3 for the mixing experiment indicated as S6 in Table 2 ($Re = 1.26 \times 10^6$). In this experiment, the impeller velocity is larger ($N = 3000$ rpm) than that in the previous experiment. As a consequence, the time

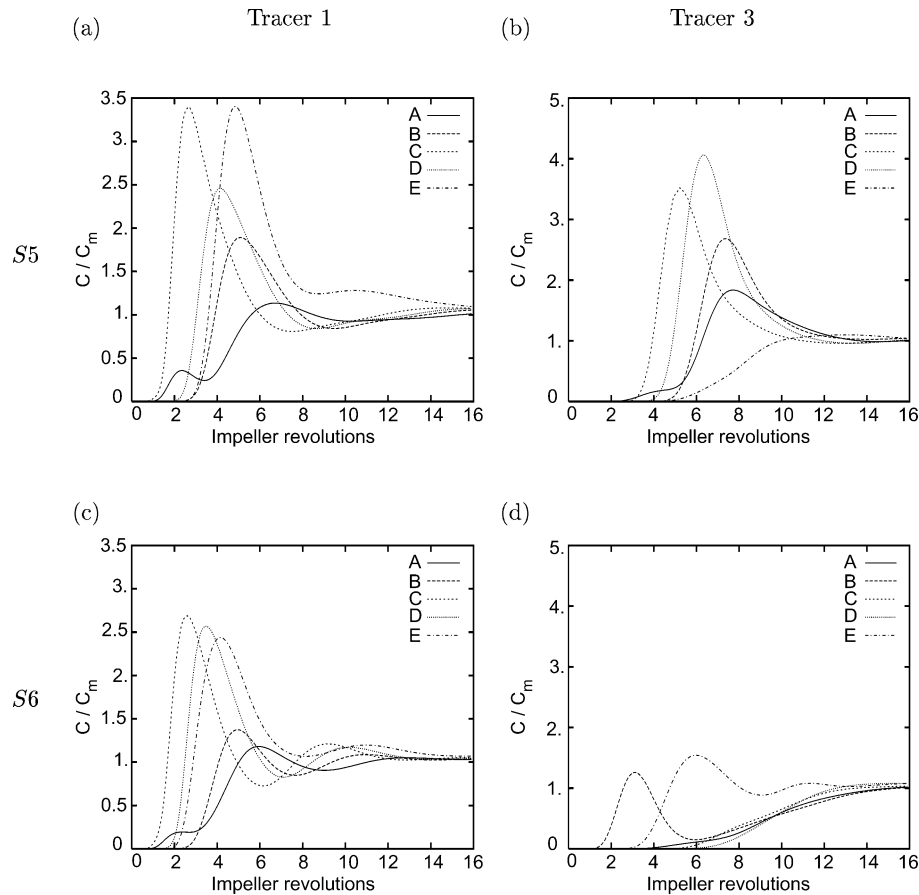


Figure 6. Evolution of concentration for different injection points and different operating conditions: (a) tracer 1, simulation S5 ($Re = 1.26 \times 10^5$), (b) tracer 3, simulation S5, (c) tracer 1, simulation S6 ($Re = 1.26 \times 10^6$), and (d) tracer 3, simulation S6.

Table 4. Mixing Time Calculated by Numerical Simulations, θ_{mix} , and by Correlations:

$\theta_{\text{mix}}^{(1)}$ Is from Holmes, Voncken, and Dekker (1964), $\theta_{\text{mix}}^{(2)}$ Is from Nienow (1997), Bulk Flow Model, and $\theta_{\text{mix}}^{(3)}$ Is from Nienow (1997), Turbulent Dispersion Model

	Re	θ_{mix} [s]	$\bar{\theta}$			$\theta_{\text{mix}}^{(1)}$	$\theta_{\text{mix}}^{(2)}$	$\theta_{\text{mix}}^{(3)}$	$\Delta\theta^{(1)}/\theta_{\text{mix}}$	$\Delta\theta^{(2)}/\theta_{\text{mix}}$	$\Delta\theta^{(3)}/\theta_{\text{mix}}$
S3	1.125×10^3	3.4	17.	3.34	7.85	2.55			-2%	+130%	-25%
S4	1.125×10^4	30.5	15.25	33.4	64.7	25.30			+10%	+112%	-17%
S5	1.125×10^5	2.9	14.5	3.34	6.56	2.53			+15%	+126%	-13%
S6	1.125×10^6	0.28	14.	0.334	0.657	0.252			+19%	+135%	-10%

scaling on the x -axis, represented by the number of impeller revolutions, corresponds to time instants different than those in Figures 6a and b. At this larger Reynolds number, concentration profiles for tracer 1 show the same qualitative trend observed in Figure 6a, whereas we observe qualitative differences for tracer 3. Concentration profiles at points B and E, located in the upper part of the vessel, show peaks which are better defined and occur earlier than that in simulation S5. In this simulation, the larger impeller velocity quickly advects the tracer in the radial direction and to the monitoring points, whereas convection to points D, C, and A is delayed.

The analysis of local concentration profiles shows that it is difficult to evaluate the mixing time from local curves. On one hand, the circulation time cannot be estimated precisely because local peaks of concentration are not always well-defined. Furthermore, for specific pairs of injection point and monitoring location, subsequent peaks of concentration are not observed. On the other hand, local concentration profiles are very sensitive to the location of injection point and it is necessary

to consider many monitoring locations simultaneously to decide when 95% of homogeneity is achieved in the tank.

In this work, we use information available for the dispersion of tracers in the overall volume of the tank to calculate the mixing time. At each time step, we identify maximum (C_{max}) and minimum values of concentration (C_{min}) in the reactor and (maximum) concentration difference, $\Delta C_{\text{max}} = C_{\text{max}} - C_{\text{min}}$. The progress of mixing is monitored by the time evolution of ΔC_{max} . At starting time, the concentration is high at the injection point and low far from the injection point, and ΔC_{max} is maximum. As mixing proceeds, ΔC_{max} reduces and finally vanishes if the tracer is perfectly mixed. In real applications, perfect mixing is seldom obtained in reasonable time. The mixing task may be considered completed when ΔC_{max} falls below a given threshold. In this work, we define θ_{mix} as the time for which $\Delta C_{\text{max}} \leq 0.1 C_m$. We account for the effect of the injection point position by comparing the values of θ_{mix} calculated for each of the three scalars, and fixing $\theta_{\text{mix}} = \max(\theta_{\text{mix},1}, \theta_{\text{mix},2}, \theta_{\text{mix},3})$.

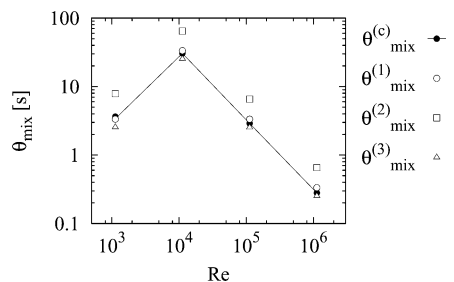


Figure 7. Mixing time calculated by numerical simulations, $\theta_{\text{mix}}^{(c)}$, and by correlations against Reynolds number, Re : $\theta_{\text{mix}}^{(1)}$ is from Holmes, Voncken, and Dekker (1964), $\theta_{\text{mix}}^{(2)}$ is from Nienow (1997), bulk flow model, and $\theta_{\text{mix}}^{(3)}$ is from Nienow (1997), turbulent dispersion model.

Table 4 shows results obtained for simulations S3–S6. We do not report data for simulations S1 and S2, performed in the laminar regime because we stopped these simulations after 30 impeller revolutions since homogeneity was not yet achieved.

Figure 7 shows values of θ_{mix} (solid symbols) against the Reynolds number. The range of variation of the dimensional mixing time spans 3 orders of magnitude for the conditions investigated. Nevertheless, as discussed by Nagata,²¹ the corresponding number of impeller revolutions, $\theta = \theta_{\text{mix}} \cdot N$, which is often referred to as the dimensionless mixing time, varies only slightly (it is 17 for S3 and 14 for S6). This indicates that, irrespective of whether the impeller speed is high or low, mixing is completed after a similar number of revolutions. Considering simulation S4, S5, and S6, corresponding to the same fluid, we observe that the mixing time reduces proportionally to the increase in impeller angular velocity.

(c) Comparison with Experimental Correlations. Results discussed in the paper can be used to *compare* (i.e., rank on a relative basis) mixing characteristics of the magnetically stirred reactor in different conditions. Precise quantitative evaluation of mixing time *must* be supported by experimental validation. We try to compare calculated mixing time against *correlations* available from the literature to mutually assess numerical results and existing correlations.

We consider the two approaches usually adopted for the interpretation of mixing data, i.e., the bulk flow model and the turbulent dispersion model.

Following the first approach, convective effects dominate and control the mixing process. We use the simple correlation proposed by Holmes, Voncken, and Dekker¹¹ to calculate the frequency of circulation as

$$f = 1.12 \cdot N \left(\frac{D}{T} \right)^2 \quad (2)$$

and we derive the circulation time as $t_c = 1/f$. Then we calculate the mixing times as $\theta_{\text{mix}}^{(1)} = 5t_c$. Table 4 compares results of our calculations against values predicted by eq 2. Values are shown in Figure 7 using white circles. As shown in Table 7, differences between values calculated numerically, θ_{mix} , and using the correlation, $\theta_{\text{mix}}^{(1)}$, are in the range 2–20%. Interestingly, the error increases with the Reynolds number, and for simulations S4–S6 the correlation predicts values of $\theta_{\text{mix}}^{(1)}$ that are slightly larger than calculated ones. As may be expected, this indicates that, in turbulent conditions, dispersion is promoted by a mech-

anism different from bulk circulation, thus reducing the mixing time.

We consider also a different correlation proposed by Nienow,¹² which has been successfully used to fit a large set of experimental data obtained from different impellers. Following ref 12, the mixing time can be predicted as a function of the circulation flow number, impeller velocity, and geometric characteristics of the impeller/vessel configuration as

$$\theta_{\text{mix}}^{(2)} = 3.926 \cdot N_{\text{qc}}^{-1} \left(\frac{D}{T} \right)^{-3} N^{-1} \quad (3)$$

Values of $\theta_{\text{mix}}^{(2)}$ predicted by eq 3 are shown in Table 4 and plotted using white squares in Figure 7. In this case, the correlation based on a bulk flow model overpredicts the mixing time by a factor of 2, indicating that turbulent dispersion should play the major role in our tank configuration.²⁴

Finally, we considered one correlation based on the turbulent dispersion model, which identifies turbulent diffusion as the step controlling the mixing process. Nienow¹² shows that, following this approach, the mixing time can be predicted as

$$\theta_{\text{mix}}^{(3)} = 5.3 \cdot Ne^{-1/3} \left(\frac{D}{T} \right)^{-2} N^{-1} \quad (4)$$

for a large number of impellers, irrespective of the shape of the impeller. In this case, mixing time is related to the power number, Ne , and therefore to energy dissipation in the tank. Values of $\theta_{\text{mix}}^{(3)}$ predicted using equation 4 are shown in Table 4 and plotted in Figure 7 using white triangles. Differences between values of θ_{mix} calculated numerically and using the correlation are in the range 10–25%. Interestingly, in this case the error decreases with the Reynolds number, and the correlation predicts values of $\theta_{\text{mix}}^{(3)}$ that are smaller than those calculated.

Present investigations show that there are significant quantitative differences in the values of mixing times predicted when correlations available from the literature are applied to the present impeller/vessel configuration. This indicates that experimental analyses on magnetic impellers are necessary, on one hand, to validate numerical calculations and, on the other hand, to improve the predicting capability of experimental correlations. Numerical results are in qualitative agreement with the same correlations. The good match with these correlations indicates that the circulation flow rate and the power input per unit mass are the *relevant physical parameters* which control the convective and dispersive transport of species, independently of the specific configuration examined.

4. Conclusions

In this work, we investigated numerically the fluid dynamics and the mixing efficiency of a tank reactor stirred by a magnetically driven impeller. MSRs are increasingly used in food and pharmaceutical industries and represent a significant proportion of the overall impeller business. Despite their economic importance, they have received little attention in the literature.

We investigated the flow field dynamics and the dispersion of species using available computational techniques to perform numerical experiments. The detailed analysis of the flow field shows that the

Table 5. Parameters for Nagata Correlation

b^* [mm]	b_{eq}/T	d/T	H/T	B_w/T	A	B	p	C	Ne_∞	Ne_{max}
32.2	0.333	0.517	1	0.1	43.84	3.97	2.346	1	0.397	3.97

circulation generated by the impeller is large and, yet, is obtained with high energy consumption due to the low off-bottom clearance. This is confirmed by the values calculated for power input, discharge flow, and secondary circulation flow. Power numbers, discharge flow numbers, and secondary circulation flow numbers, compared with values calculated for energy efficient, shaft-driven impellers, indicate that significant stirring is obtained but at a large power expense.

We simulated also the dispersion of species, considering the effect of different injection points on the mixing dynamics. First, we analyzed in detail the three-dimensional evolution of blotches of tracer, linking the dispersion behavior to the time-dependent flow field. Second, we evaluated the mixing time. We show that the approach customarily used in experiments, based on the analysis of the evolution of local concentration profiles, may produce inaccurate results when specific pairs of injection points and monitoring points are chosen. We propose a different approach to quantify the mixing time, which is independent of injection point and monitoring point locations.

Finally, we compared values of mixing time calculated numerically with values predicted by correlations derived for traditional mixers. We find that numerical results are in qualitative agreement with both bulk flow models and turbulent dispersion models. Yet it is necessary to perform experimental investigations on MSR (i) to improve the predictive ability of experimental correlations and (ii) to obtain data for the validation of numerical investigations.

Acknowledgment

We wish to thank Cristian Talotti and Alessandro Agosto for performing some numerical simulations. Special thanks to Ing. Mariotti and Mr. Pecini from Mariotti e Pecini s.r.l. for their useful and kind suggestions and for economical support, and to Polo Tecnologico 'La Magona', Cecina (Livorno, Italy). The MIUR contribution under Grant PRIN 2003099224_002 is gratefully acknowledged. One of the authors (M.C.) is grateful for the European Union support under ICOPAC grant UE-HPRN_CT-2000-00136.

Appendix

Empirical Correlations. The general form of the power characteristic (see Nagata²¹) is

$$Ne = \frac{A}{Re} + B \left(\frac{10^3 + 0.6 \cdot f \cdot Re^\alpha}{10^3 + 1.6 \cdot f \cdot Re^\alpha} \right)^p \quad (5)$$

The first term represents the power consumption in the laminar range and the second term represents the power consumption in the turbulent range. The coefficients of the empirical equation, A , B , p , f , and α , are estimated from the geometrical characteristics of the stirred tank reactor using the correlations experimentally derived from the data collected for a simple

configuration (single-paddle impeller, $H/T = 1$, vertical blades, i.e., $\theta = 90^\circ$):

$$A = 14 + \frac{b}{T} \left[670 \cdot \left(\frac{D}{T} - 0.6 \right)^2 + 85 \right] \quad (6)$$

$$B = 10^{[1.3 - 4 \cdot ((b/T) - 0.5)^2 - 1.14(D/T)]} \quad (7)$$

$$p = 1.1 + 4 \cdot \frac{b}{T} - 2.5 \left(\frac{D}{T} - 0.5 \right)^5 - 7 \left(\frac{b}{T} \right)^4 \quad (8)$$

$$f = 2 \quad \alpha = 0.66 \quad (9)$$

Many corrections are needed for stirred tank reactors having a different configuration:

1. Effect of a different number of paddles and of a different type of impeller: an equivalent blade height, $b_{eq} = b^* \cdot n_p$, is used instead of b , and the number of paddles, n_p , is calculated from the number of blades. Specifically, each blade is equivalent to 0.5 paddles and b^* is calculated as the height of a paddle having the same diameter of the real impeller, D , and the same momentum of the impeller section with respect to the rotation axis. With reference to quantities indicated in Figure 1a, b^* may be calculated as

blade area · offset from rotation axis =

$$b^* \cdot \frac{D \cdot D}{2 \cdot 4} = b \cdot \frac{D - D_h}{2} \cdot \left(\frac{D}{2} - \frac{D - D_h}{4} \right) \quad (10)$$

2. Effect of liquid depth: a multiplicative factor C is used for the turbulent contribution to the power consumption

$$C = \left(\frac{H}{T} \right)^{0.35 + (b/T)} \quad (11)$$

3. Effect of the blade inclination (θ): a multiplicative factor C_1 is used for the turbulent contribution to the power consumption

$$C_1 = (\sin \theta)^{1.2} \quad (12)$$

4. Effect of baffles: the geometrical characteristics of the baffles are used to determine the asymptotic value for the power dissipation, corresponding to

(a) "Fully baffled" condition

$$\left(\frac{B_w}{T} \right)^{1.2} \cdot n_B = 0.35 \quad (13)$$

corresponding to the maximum power consumption, Ne_{max} , given by

$$Ne_{max} = \frac{A}{Re} + B \cdot C \quad (14)$$

(b) Partially baffled conditions, corresponding to a power number, Ne_B , given by

$$\frac{Ne_{max} - Ne_B}{Ne_{max} - Ne_\infty} = \left[1 - 2.9 \left(\frac{B_w}{T} \right)^{1.2} n_B \right]^2 \quad (15)$$

where the power number obtained at Re tending to infinity, Ne_∞ , is given by

$$Ne_\infty = B \left(\frac{0.6}{1.6} \right)^p \quad (16)$$

Correction factors are used to define the following curves:

1. The "no baffle" curve

$$Ne = \frac{A}{Re} + B \left(\frac{10^3 + 0.6 \cdot f Re^\alpha}{10^3 + 1.6 \cdot f Re^\alpha} \right)^p \quad (17)$$

2. The "baffled" curve

$$Ne = \frac{A}{Re} + B \cdot C \cdot C_1 \cdot \frac{Ne_B (10^3 + 0.6 \cdot f Re^\alpha)^p}{Ne_\infty (10^3 + 1.6 \cdot f Re^\alpha)^p} \quad (18)$$

3. The "fully baffled" curve

$$Ne = \frac{A}{Re} + B \cdot \frac{Ne_{\max} (10^3 + 0.6 \cdot f Re^\alpha)^p}{Ne_\infty (10^3 + 1.6 \cdot f Re^\alpha)^p} \quad (19)$$

Dimensionless geometric parameters derived for the configuration examined are gathered in Table 5. These values are used to calculate the correlation parameters and to obtain the functional representation of the power characteristic shown in Figure 3.

Literature Cited

- (1) Derksen, J. J.; Van den Akker, H. E. A. Large-eddy simulations on the flow driven by a Rushton turbine. *AIChE J.* **2000**, *45*, 209.
- (2) Verzicco, R.; Fatica, M.; Iaccarino, G.; Orlandi, P. Flow in an impeller-stirred tank using an immersed boundary method. *AIChE J.* **2004**, *50*, 1109.
- (3) Bakker, A.; Haidari, A. H.; Oshinowo, L. M. Realize Greater Benefits from CFD. *Chem. Eng. Prog.* **2001**, *97*, 45.
- (4) Campolo, M.; Sbrizzai, F.; Soldati, A. Time-dependent flow structures and Lagrangian mixing in Rushton-impeller baffled-tank reactor. *Chem. Eng. Sci.* **2003**, *58*, 1615.
- (5) Patwardhan, A. W.; Joshi, J. B. Relation between flow pattern and blending in stirred tanks. *Ind. Eng. Chem. Res.* **1999**, *38*, 3131.
- (6) Brucato, A.; Ciofalo, M.; Grisafi, F.; Tocco, R. On the simulation of stirred tank reactors via computational fluid dynamics. *Chem. Eng. Sci.* **2000**, *55*, 291.
- (7) Harvey, A.; Rogers, S. E. Steady and unsteady computation of impeller stirred reactors. *AIChE J.* **1996**, *42*, 2701.
- (8) De La Villeon, J.; Bertrand, F.; Tanguy, P. A.; Labrie, R.; Bousquet, J.; Lebouvier, D. Numerical investigation of mixing efficiency of helical ribbons. *AIChE J.* **1998**, *44*, 972.
- (9) Delaplace, G.; Leuliet, J. C.; Relandeau, V. Circulation and mixing times for helical ribbon impellers. Review and experiments. *Exp. Fluids* **2000**, *28*, 170.
- (10) Lamberto, D. J.; Alvarez, M. M.; Muzzio, F. J. Computational analysis of regular and chaotic mixing in a stirred tank reactor. *Chem. Eng. Sci.* **2001**, *56*, 4887.
- (11) Holmes, D. B.; Voncken, R. M.; Dekker, J. A. Fluid flow in turbine-stirred, baffled-tank-I: Circulation time. *Chem. Eng. Sci.* **1964**, *19*, 201.
- (12) Nienow, A. W. On impeller circulation and mixing effectiveness in the turbulent flow regime. *Chem. Eng. Sci.* **1997**, *52*, 2557.
- (13) Rushton, H. J. Applications of fluid mechanics and similitude to scale-up problems. Part 1. *Chem. Eng. Prog.* **1952**, *48*, 33.
- (14) Bartels, C.; Breuer, M.; Durst, F. Comparison between direct numerical simulation and $k - \epsilon$ prediction of the flow in a vessel stirred by a Rushton turbine. *Proc. 10th Eur. Conf. Mixing* **2000**, 239.
- (15) Sahu, A. K.; Joshi, J. B. Simulation of flow in stirred vessel with axial flow impellers: Effects of various numerical schemes and turbulence model parameters. *Ind. Eng. Chem. Res.* **1995**, *34*, 626.
- (16) Campolo, M.; Paglianti, A.; Soldati, A. Fluid dynamic efficiency and scale-up of a retreated blade impeller CSTR. *Ind. Eng. Chem. Res.* **2002**, *41*, 164.
- (17) Luo, J. Y.; Issa, R. I.; Gosman, A. D. Prediction of impeller-induced flow in mixing vessels using multiple frame of reference. *ICHEME Trans.* **1994**, *136*, 549.
- (18) Serra, A.; Campolo, M.; Soldati, A. Time-dependent finite-volume simulation of the turbulent flow in a free-surface CSTR. *Chem. Eng. Sci.* **2001**, *56*, 2715.
- (19) Armenante, P. M.; Mazzarotta, B.; Chang, G. Power consumption in stirred tanks provided with multiple pitched-blade turbines. *Ind. Eng. Chem. Res.* **1999**, *38*, 2809.
- (20) Armenante, P. M.; Chou, C. C. Velocity profiles in a baffled vessel with single or double pitched-blade turbines. *AIChE J.* **1996**, *42*, 42.
- (21) Nagata, S. *Mixing: Principles and Applications*; Kodansha, Tokyo, Japan, 1975.
- (22) Campolo, M.; Soldati, A. Appraisal of fluid dynamic efficiency of retreated blade and turbofoil impellers in industrial size CSTRs. *Ind. Eng. Chem. Res.* **2002**, *41*, 1370.
- (23) Lamberto, D. J.; Alvarez, M. M.; Muzzio, F. J. Experimental and computational investigation of the laminar flow structure in a stirred tank. *Chem. Eng. Sci.* **1999**, *54*, 919.
- (24) Patwardhan, A. W.; Pandit, A. B.; Joshi, J. B. The role of convection and turbulent dispersion in blending. *Chem. Eng. Sci.* **2003**, *58*, 2951.

Received for review January 20, 2004
 Revised manuscript received July 21, 2004
 Accepted August 12, 2004

IE0499355